Ultramicroscopy 187 (2018) 98–106

Contents lists available at ScienceDirect

Ultramicroscopy

journal homepage: www.elsevier.com/locate/ultramic

Energy-weighted dynamical scattering simulations of electron diffraction modalities in the scanning electron microscope

Elena Pascal[a], Saransh Singh[b], Patrick G. Callahan[c], Ben Hourahine[a], Carol Trager-Cowan[a], Marc De Graef[b,*]

[a] Department of Physics, SUPA, University of Strathclyde, G4 0NG, Glasgow, UK
[b] Department of Materials Science and Engineering, Carnegie Mellon University, Pittsburgh, PA 15213-3890, USA
[c] Department of Materials, University of California at Santa Barbara, Santa Barbara, CA 93106, USA

ARTICLE INFO

Article history:
Received 23 October 2017
Revised 21 December 2017
Accepted 17 January 2018
Available online 2 February 2018

Keywords:
Transmission Kikuchi diffraction
TKD
Dynamical simulations
Monte Carlo
Dictionary indexing

ABSTRACT

Transmission Kikuchi diffraction (TKD) has been gaining momentum as a high resolution alternative to electron back-scattered diffraction (EBSD), adding to the existing electron diffraction modalities in the scanning electron microscope (SEM). The image simulation of any of these measurement techniques requires an energy dependent diffraction model for which, in turn, knowledge of electron energies and diffraction distances distributions is required. We identify the sample-detector geometry and the effect of inelastic events on the diffracting electron beam as the important factors to be considered when predicting these distributions. However, tractable models taking into account inelastic scattering explicitly are lacking. In this study, we expand the Monte Carlo (MC) energy-weighting dynamical simulations models used for EBSD [1] and ECP [2] to the TKD case. We show that the foil thickness in TKD can be used as a means of energy filtering and compare band sharpness in the different modalities. The current model is shown to correctly predict TKD patterns and, through the dictionary indexing approach, to produce higher quality indexed TKD maps than conventional Hough transform approach, especially close to grain boundaries.

1. Introduction

Electron diffraction techniques in the scanning electron microscope (SEM) are established and versatile tools for microstructural investigation of crystalline materials. The strong and complex local interactions of electrons with crystalline matter offer a plethora of information about the crystal structure and material properties of a sample that can be recovered from the recorded signal. A review of these is given in ref. [3]. Kikuchi patterns are one representation of the diffracting behaviour of electrons in the form of a variation in the angular distribution of signal electrons. The geometry of these patterns is dictated by the unit cell of the crystal and its orientation. Other features, such as the width of the bands, for instance, are nevertheless influenced by the spatial distribution of electrons in the sample and their energy distribution (for a more complete discussion see ref. [4]).

We can distinguish a number of different SEM modalities employing the Kikuchi diffraction mechanism. If the recorded electrons are the backscattered ones (BSEs), then the technique is known as electron backscatter diffraction (EBSD) and the Kikuchi patterns obtained are called electron backscatter patterns (EBSP). Automated pattern indexing software established this diffraction modality as one of the conventional tools of orientation mapping, phase identification and/or relative lattice strain estimation in crystalline materials [3]. In order to increase the diffraction signal in this mode, the popular approach has been to tilt the sample to about 70° from horizontal towards the detector, which guarantees a maximum backscattered electron yield. However, the high tilt will also spread out the information volume (or interaction volume) of the electrons within the sample, resulting in limitation of the achievable spatial resolution.

Stimulated by the increased attention to nanostructured materials, which promise new and enhanced properties when compared to their larger scale counterparts, the interest in improving the resolution of established characterization techniques has also

* Corresponding author.
E-mail addresses: elena.pascal@strath.ac.uk (E. Pascal), ssaransh@andrew.cmu.edu (S. Singh), pcallahan@ucsb.edu (P.G. Callahan), benjamin.hourahine@strath.ac.uk (B. Hourahine), c.trager-cowan@strath.ac.uk (C. Trager-Cowan), degraef@cmu.edu (M.D. Graef).

https://doi.org/10.1016/j.ultramic.2018.01.003

expanded. The use of forward-scattered electrons (FSEs) through a thin sample as diffraction signal collected from the bottom of the foil has been shown to improve the lateral spatial resolution to below 10 nm [5,6]; this technique is commonly known as transmission Kikuchi diffraction (TKD) or transmission EBSD (t-EBSD).

The modalities above are sometimes referred to as "channeling out" diffraction techniques [7] to suggest that the diffraction information has been sampled by electrons on their way out of the sample and that the volume from which the signal is collected is located close to the exit surface. The SEM can also be used in "channeling in" mode when electron channeling patterns (ECPs) are acquired [8,9]. In this case, Kikuchi-like diffraction patterns can also be obtained by varying the incident beam direction with respect to the crystal. Typically, those patterns have a smaller solid angle compared to their EBSD counterparts. Nevertheless, the physical scattering mechanisms that produce EBSPs and ECPs are related through the reciprocity principle [10].

Theoretical models have been developed and successfully applied to retrieve this wealth of information by taking into account the full dynamical behaviour of electron diffraction [11–13]. Electron diffraction calculations commonly handle inelastic scattering in a phenomenological way through the introduction of a complex optical crystal potential approximation. This assumption implies that inelastically scattered electrons, once they lose even a small amount of energy, will cease to contribute to the diffraction pattern. The predicted diffraction patterns based on this simplified model remain meaningful [14] but, understandably, are lacking quantitative precision. Due to the strong interaction of incident beam electrons at SEM energies with matter, the inelastic cross section is always comparable to the elastic one, and a portion of inelastically scattered electrons will reach the detector and contributes to the imaged pattern.

Depending on the types of inelastic channels allowed, these electrons can suffer diffraction after losing a small amount of energy, contributing then to the diffuseness of the Kikuchi patterns. This process is especially relevant for "channelling out" modalities where electrons with energies lower than the incident energy can still contribute to the diffraction pattern. Alternatively, if electrons are scattered at a large angle multiple times such that memory of their original direction is lost, they will also contribute to the background intensity. This is the case for both channeling modalities. We call the later type of inelastically (back/forward-)scattered electrons (B/F)SE2 in order to differentiate them from (B/F)SE1 electrons carrying diffraction information.

It is therefore essential to explicitly consider inelastic scattering and its effects on the signal contributing electrons, such as their energy and spatial distributions [1,15]. This is especially important if finer features of the Kikuchi bands (size, absolute intensity relative to background, band edges) are to be correctly predicted. A full account of the inelastic channels in electron diffraction poses a challenging problem. While general Schrödinger equation solutions for inelastic scattering in perfect crystals have been proposed by Yoshioka [16] and solved for various electron microscopy applications (see Howie [14] for small angle plasmon scattering and Forbes et al. [17] for single thermal diffuse scattering events), to our knowledge, readily implementable solutions relevant for SEM electron energies have yet to be proposed.

In this work, we assume inelastic scattering events to be stochastic and that Monte Carlo (MC) techniques can estimate both the trajectories of electrons that suffered such events as well as their energy distribution. Such models have been proposed and widely used to correctly predict distributions of backscattered electrons [18]. The assumption that the distributions of escape energies and trajectories of electrons carrying diffraction information can be estimated from the last elastic event predicted by MC models has already been successfully applied for EBSPs [1] and ECPs [2]. The electron energy at the last elastic event, prior to leaving the sample, is regarded as the diffraction energy (energy at which the diffraction event occurs), and the distance to the exit surface from the elastic event (escape or exit distance) is used as the diffraction distance (electron path length over which coherence is not lost). Dynamical diffraction modelling is then applied for the full MC predicted electron energy and path distributions. Here, we extend this model to TKD patterns by considering the geometry of a thin film sample where the entry (top) and escape (bottom) surfaces are different such that the incoherent events acting as sources of diffracting electrons are scattering in a forward direction.

While this approach may not take into account the full extent of inelastic scattering effects on diffracted electrons proposed by the Yoshioka equations, it leads to a model of manageable complexity which is straightforward to implement and whose predictions are easily understood. Most importantly, it represents a step forward in taking into account the full physics of electron diffraction in matter by considering the full distribution of energies of channeling electrons and produces accurate predictions when compared to experimental patterns, as shown in Section 3.2.

In Section 2 we describe the typical geometries for EBSD, TKD and ECP data acquisition and formulate a general expression for the thickness integrated back-scattered electron intensity that is applicable to all three diffraction modalities. We describe the particulars of the Monte Carlo trajectory simulations in Section 2.2, along with the resulting differences between the modalities. Master patterns for the three modalities are described and compared in Section 3.1. In Section 3.2 we compare experimental and simulated TKD patterns, and Section 3.3 illustrates how the recently developed dictionary indexing technique [19] can be applied to TKD patterns. We conclude the paper with a brief discussion and summary in Section 4.

2. Theoretical model

2.1. Energy and diffraction distance integrated electron intensity

The simulation of the (back/forward-)scattered electron distribution emerging from a sample illuminated with a fine, nearly-parallel, electron probe can be achieved in general by integrating over both the energy range of the exiting electrons and the distance traveled in the sample between the scattering site and the sample surface. The probability of a (B/F)SE emerging from the sample in the direction $\hat{\mathbf{k}}$ (the hat indicates a unit vector) can be written as follows:

$$P(\hat{\mathbf{k}}) = \sum_{n \in \text{A.U.}} P_n(\hat{\mathbf{k}}), \tag{1}$$

where A.U. stands for asymmetric (primitive) unit and the index n runs over all positions in the asymmetric unit. The probability P_n is defined as:

$$P_n(\hat{\mathbf{k}}) = \sum_{j \in \mathcal{S}_n} \sigma_j \int_{E_{\min}}^{E_{\max}} \mathrm{d}E \int_0^{t_0(E)} \mathrm{d}t\, \bar{\lambda}_{\hat{\mathbf{k}}}(E,t) |\Psi_{\hat{\mathbf{k}}}(\mathbf{r}_j; E, t)|^2. \tag{2}$$

Here, $\sigma_j = Z_j^2 D_j$ (with Z the atomic number and D the Debye–Waller factor) is the Rutherford scattering cross section for atom j in the set of equivalent positions $\mathcal{S}_n$; $E_{\max}$ is the maximum energy (potentially the incident beam energy E_0) and $E_{\min}$ the lowest energy considered in the calculation; t is the distance between the scattering site and the sample surface, measured along the exit direction; $t_0(E)$ is the maximum distance to be considered; $\bar{\lambda}_{\hat{\mathbf{k}}}(E,t)$ is a weighting function describing the fraction of incident electrons (per unit energy and per unit length) of energy E, originating a distance t from the sample surface and traveling in the direction $\hat{\mathbf{k}}$; the wave function $\Psi_{\hat{\mathbf{k}}}$ is evaluated for the equivalent atom positions $\mathbf{r}_j$ and the parameters E and t. For the latter, one can use ei-

ther the Bloch wave approach or the scattering matrix formalism. The weighting function $\bar{\lambda}$ is defined as:

$$\bar{\lambda}_{\hat{\mathbf{k}}}(E,t) \equiv \frac{\lambda_{\hat{\mathbf{k}}}(E,t)}{Nt_0(E)(E_{\max}-E_{\min})}, \quad (3)$$

where $\lambda_{\hat{\mathbf{k}}}(E,t)$ represents an energy-depth-direction distribution obtained from Monte Carlo (MC) simulations, to be discussed in the following section, and N is the total number of incident beam electrons. The normalization factor in the denominator renders the integrations in Eq. (2) dimensionless.

Eq. (2) is valid for all (B/F)SE diffraction modalities, including EBSD, ECP and TKD. The differences between them lie in the nature of the sample (bulk vs. thin foil), the geometry of the scattering process (back-scattering vs. forward scattering), and the subset of electrons carrying the coherent diffraction signal (all backscattered electrons vs. (B/F)SE1 electrons). These differences will be encoded in the geometry dependent weighting function $\bar{\lambda}$ for each of the modalities.

The Monte Carlo model enables us to predict how any of these system parameters influence the form of the weighting function. For instance, in the next section we discuss the impact of different sample geometries on TKD patterns, while in Section 2.3 the effect of foil thickness is investigated. Then, in Section 2.4 the sample-detector geometry is considered as a useful system parameter that can identify special cases for which the numerical solution of the scattering process can be simplified dramatically via the use of so-called *master patterns*.

2.2. Monte Carlo trajectory simulations

The use of Monte Carlo simulations in predicting energy and spatial distribution of diffracting electrons has been described before for EBSPs [1] and ECPs [2] on bulk samples. These simulations employ Joy and Luo's [20] modified version of Bethe's continuous slowing down approximation (CSDA) as an empirical estimation for a sum of inelastic scattering processes probabilities. The probabilities of elastic scattering events are determined from the Rutherford scattering cross section in the single scattering approximation. Therefore, the loss of energy is uniquely determined by the CSDA while the angular deflections from the original direction are defined by the elastic scattering events. For further details on this simulation approach we refer to the book by Joy [18].

We apply a similar approach for the TKD modality with the modification that the sample is now a thin film and the escape surface is not the same as the entry one. A collimated beam of electrons at incident beam energy enter the top surface and start both losing energy and scattering away from their original trajectories. Eventually they will suffer one final forward-scattering event after which they will diffract on their way out of the bottom sample surface and reach the detector. The energy and depth distributions for each scattering direction of this last event is predicted using the MC model since all events leading to it can be assumed to be stochastic. These distributions are then binned for easy storage and used as estimated values of the weighing function $\bar{\lambda}_{\hat{\mathbf{k}}}(E,t)$.

Additionally, the Monte Carlo model can be used to predict general electron trajectories inside the sample and the system parameters that might affect them. In Fig. 1 we show angular (directional) distributions of escaping electrons predicted by the MC model for the TKD modality. The intensities are shown as stereographic projections (SPs) in the sample's southern hemisphere for a beam of 20 keV electrons incident on a 200 nm thick Ni foil. By binning the energy values of the electrons escaping from the bottom of the foil into high loss energy electrons (escape energy (E_e) < 17.5 keV), medium loss electrons (17.5 keV $\leq E_e < 18.5$ keV) and low-loss energy electrons ($E_e > 18.5$ keV) we can show the effect of energy filtering and observe the behaviour of different energy electrons.

Fig. 1(a) shows projections for the case when the sample is horizontal and the electron beam normal. Here we can observe, as expected, that higher energy transmitted electrons are much more focused in the middle of the southern hemisphere, which happens to coincide with the direction of the incident beam. With increased energy loss we can observe an increase in trajectory randomization or diffuseness. This can be explained by considering the possible trajectories of electrons inside the sample and their corresponding energy loss. Electrons escaping the sample with energies close to the incident beam will not have deviated far from the incident direction. Relative to this, high loss electrons are more likely to escape at large angles to their incident direction. Very high energy loss electrons appear to have no preferred escape direction and we can expect these electrons to only contribute to image background (FSE2).

In Fig. 1(b) we investigate the effect of tilting the sample on the angular distribution of exiting electrons from the bottom surface. Similarly, the high energy electrons will not deviate far from their incident trajectories. However, in this case, the incident direction does not correspond to the center of the SP space and we observe that the directional distribution of the low loss electrons clusters 30° below the SP horizon. The trajectories of higher loss electrons start to be randomized in the entire SP space. We can also observe in these images how the radial symmetry of electron scattering is broken by the tilt angle of the sample. Finally, the angular distribution of the highest loss electron distribution will look the same as for the flat sample as their "memory" of the incident direction is lost.

The outline in the rightmost column of Fig. 1(a) and (b) depicts a typical detector projected onto the stereographic disk. The detector has dimensions 24×36 mm^2 and is inclined by 10° from the vertical direction. The perpendicular distance from the exit point on the bottom of the sample to the detector is 20 mm, and the top edge of the detector lies in the sample plane for the 0° orientation. The detector bottom is closest to the center of the stereographic projection. For 0° sample tilt, most of the scattered electrons miss the detector surface; for a $-30°$ sample tilt, the intensity maximum moves upwards onto the lower part of the detector and at the same time the detector projection moves closer to the center of the stereographic disk, indicating that a significantly larger number of electrons will reach the scintillator. It should also be noted that a typical raw TKD pattern will display a rather steep intensity gradient from top to bottom, in agreement with the intensity distribution inside the detector outline in Fig. 1(b) (rightmost image).

It becomes apparent that the sample geometry constitutes an important parameter in the formation of the Kikuchi patterns. Similarly to the EBSD case, where the sample tilt determines the preferred trajectories of electrons of different energies scattering back from the sample [1], the tilt of the thin film in TKD will directly influence the angular distribution of transmitted electrons suffering diffraction at different energies. In the following section we will carefully review the effect of another system parameter, the sample thickness, on the TKD diffraction patterns.

2.3. Sample thickness in TKD

While for the EBSD and ECP modalities one only needs to run a single Monte Carlo simulation to obtain the energy-depth-direction histogram $\bar{\lambda}_{\mathbf{k}}(E,t)$ for a bulk sample, for the TKD case, the MC simulation results depend on the thickness, t, of the sample. The larger the thickness, the more energy an electron will lose on its way to the exit surface, and this will shift the entire exit energy distribution to lower energies for increasing sample thickness.

This behaviour is shown in Fig. 2 as kernel density estimate (KDE) distributions [21] of electron escape energy versus escape distance predicted information for two different Ni thin foil thick-

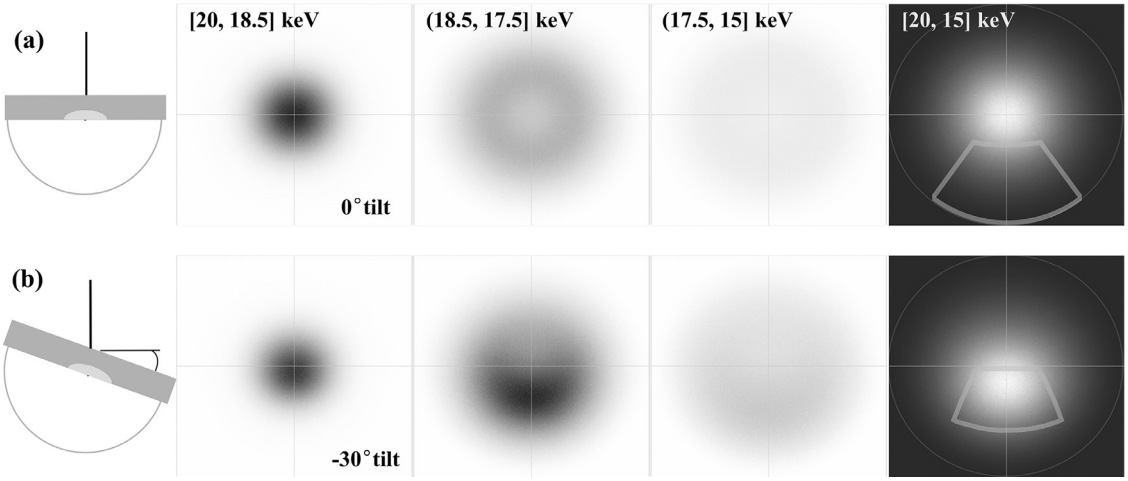

Fig. 1. Directional distributions of transmitted electrons intensity in TKD geometry for two sample tilts (shown in the first column): 0° (a) and −30° (b). The intensities are shown here as stereographic projections where the intersection of the horizontal and vertical lines indicate the middle of the space (vertical line is the semicircle in the sketch). The first three images in each case are showing "energy filtered" electron intensities (reversed contrast) while the last column displays the total intensity distribution.

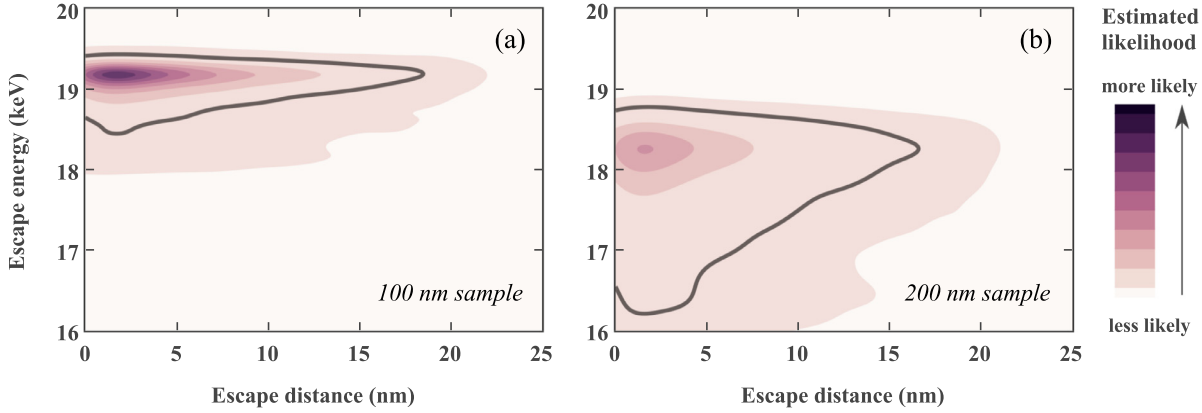

Fig. 2. KDE plots of electron energy versus escape distance distributions as predicted by the MC model for TKD geometry for two sample thicknesses (a) 100 nm and (b) 200 nm. The area enclosed by the thick line contains 90% of events. See text for further details.

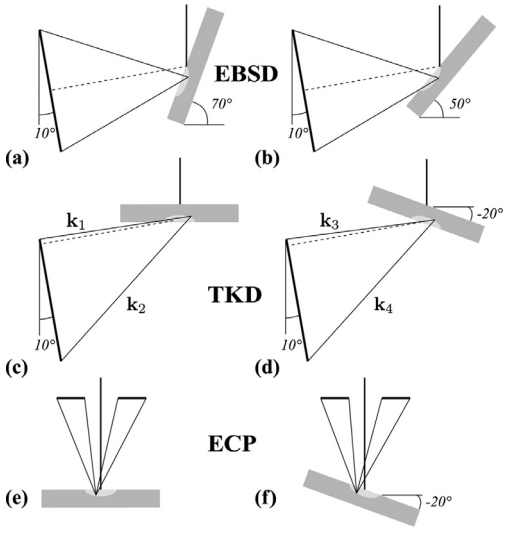

Fig. 3. (a) and (b) EBSD geometry, with the sample inclined at 70° and 50°; the detector is indicated by a thick line and is inclined by 10° with respect to the vertical direction. (c) and (d) show typical TKD geometries with a horizontal sample, and one inclined at −20°. Different **k** directions are indicated for which energy-distance KDEs distributions are shown in Fig. 4. (e) and (f) show typical ECP geometries with two different sample tilt angles.

nesses, 100 nm and 200 nm respectively, in the TKD geometry. Darker colours show that more electrons are likely to escape the sample with the corresponding parameters. The likelihood intensity across the two images has been normalized to the maximum value in Fig. 2(a) such that the intensity across images can be compared. We also show the escape energy and distance region where 90% of electrons are expected to come from, which is indicated by the thick line. Comparing the two figures, 2(a) and (b), it is clear that the thickness of the thin sample strongly influences the shape of the distributions. Considering the y-axis, the energy range of the electrons exiting the sample broadens and the energy decreases to significantly lower values as the thickness of the film increases. These observations already indicate that we should expect more diffuse diffraction patterns from thicker samples when compared to thinner ones. In general, the greater the interaction volume of electrons with the sample, the more energy will be lost by electrons before diffraction and the greater the diffuseness of the Kikuchi patterns; as supported by literature [22].

Considering the *x*-axis, we observe that the escape depth profile resembles the usual power-law distribution [15] with the bulk of the electrons carrying diffraction information originating from a few nm below the escape surface. It should be noted, that the MC model used in this study does not aim to predict the full depth of diffracting electrons or interaction volume. Instead, we make the assumption that the mean value of the full diffraction depth distribution can be estimated to be of the same order as the electron

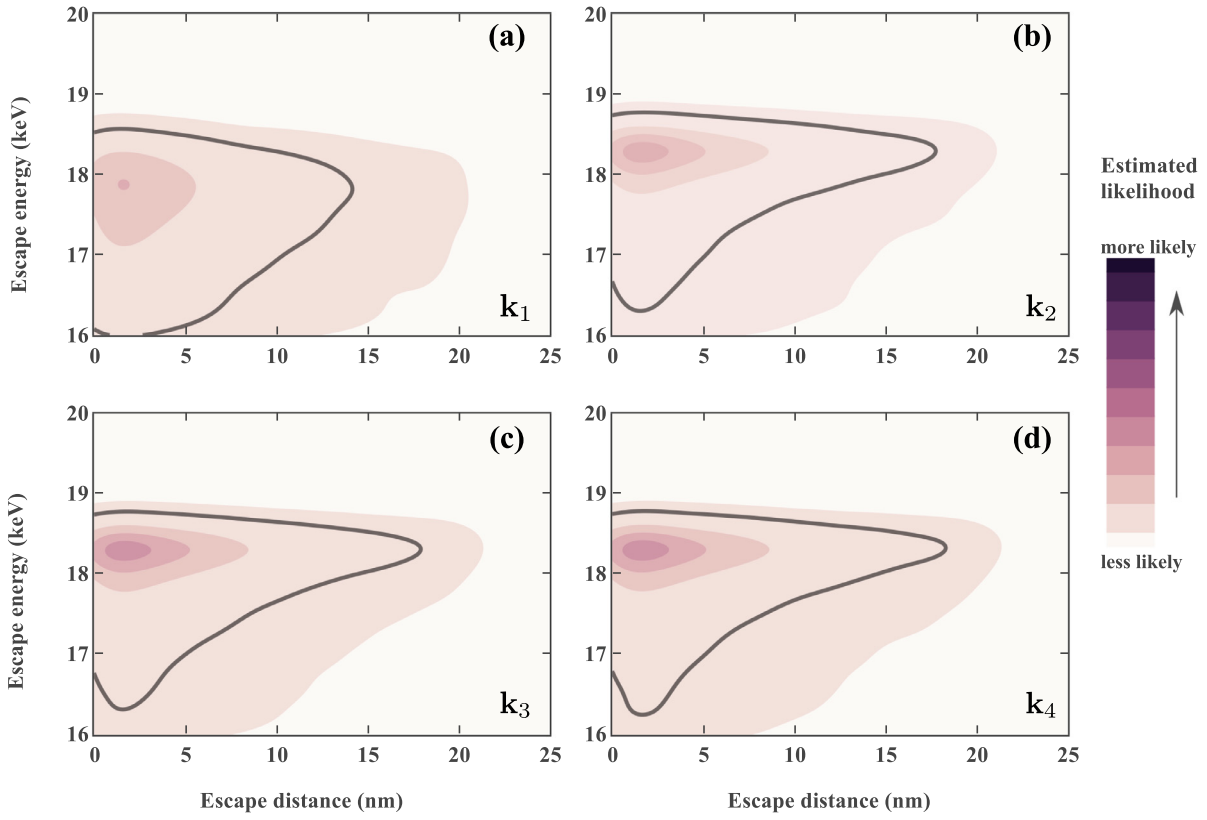

Fig. 4. KDE plots of electron energy versus escape distance distributions as predicted by the Monte Carlo model for TKD geometries and directions $\mathbf{k_i}$ shown in Fig. 3(c) and (d). The area enclosed by the thick line contains 90% of the events.

mean free path. Due to the power-law distribution rule, we can be confident that the vast majority of escape depths is considered in this model.

By comparing the two images in Fig. 2, it should be clear that accounting for the effect of sample thickness is essential when predicting accurate electron transmission diffraction patterns. In this model this is achieved by sampling the above likelihood distribution bin-wise and constructing the $\bar{\lambda}_{\mathbf{k}}(E, z)$ weighting function as discussed in Section 2.1.

In the next section, we will investigate special geometries for which electrons reaching different regions of the detector can be described by the same $\lambda_{\hat{\mathbf{k}}}(E, t)$ function, simplifying the calculations significantly.

2.4. Special sample-detector geometries and the master pattern

Consider the sample and detector geometries shown in Fig. 3(a–f) where the lighter region on the samples depicts the volume in which electrons suffer scatter events. The top row shows two potential EBSD geometries, one with the sample tilted at the standard 70° angle with respect to the horizontal plane, the other with the sample tilted at 50°. As previously discussed, the sample geometry will determine the manner in which the scattering radial symmetry will be broken. Nevertheless, the region of SP space sampled by the position of the detector will also influence the uniformity (or lack thereof) of the electron energies and diffraction distances distributions. In Fig. 3(a), the electrons that reach the top and bottom of the detector (thick line on the left, inclined at 10° from vertical) ought to have travelled approximately the same length inside the sample before channelling out; in Fig. 3(b) on the other hand, the electrons that reach the bottom of the detector have traveled a significantly larger distance inside the sample.

In TKD, the situation is similar: in Fig. 3(c) the sample is horizontal and electrons that reach the top of the detector have traveled a much larger distance inside the sample before diffracting than electrons that reach the bottom. In the top row of Fig. 4, the escape energy-escape distance distributions are shown as KDE plots for electrons reaching the top (a) and the bottom (b) of the detector. We can observe qualitative differences in these distributions, especially for the escape energies. The electrons that travelled larger distances before diffracted lost more energy and therefore their energy distribution is shifted towards lower values. On the other hand, a small sample tilt of −30° shown in (d) reduces these differences. Fig. 4 (bottom row) shows that the energy-distance distribution of electrons reaching the top of the detector (c) and the distribution of those reaching the bottom of the detector (d) is qualitatively the same. Note that Fig. 4 (b)–(d) show similar distributions since all possible trajectories $\mathbf{k_2}$, $\mathbf{k_3}$, $\mathbf{k_4}$ have similar lengths in the sample.

Finally, for the ECP case illustrated in Fig. 3(e) and (f), a small sample tilt does not significantly change the distribution of path lengths inside the sample, and most trajectories have about the same path length.

This observation has consequences for the numerical approach to be used to obtain high quality simulated patterns. For special geometries, we can now approximate the weighting function $\bar{\lambda}$ by an effective (averaged) weighting function,

$$\bar{\lambda}_{\hat{\mathbf{k}}}(E, t) \rightarrow \bar{\lambda}(E, t), \tag{4}$$

which no longer depends on the electron direction $\mathbf{k}$. This has significant advantages numerically, since one can now pre-compute the probabilities $P(\mathbf{k})$ for a spherical sampling of incident beam orientations and store the resulting BSE yields in a master pattern (MP) that can be used to generate individual EBSD/TKD patterns by

means of bi-linear interpolation, a fast and efficient way to compute many patterns in a short amount of time.

For EBSD and TKD simulations and sample orientations that deviate significantly from the standard orientations, one can not apply the above approximation, since the range of distances traveled inside the sample is quite broad; thus, in these cases one must carry out the integrations of Eq. (2) for each individual EBSD/TKD pattern, which results in a slow computational tool.

For ECPs, the situation is quite different, since only BSE1 electrons carry coherent diffraction information; all other (BSE2) electrons only contribute to the background intensity. A BSE1 electron has nearly the same exit energy as the incident electron since the Rutherford backscatter event is the first major scattering event after entering the sample. Therefore, nearly all BSE1 electrons have the same exit energy and the energy integration can be eliminated, leading to the following expression which is valid for the ECP case only (with E_0 the incident electron energy):

$$P_n^{\mathrm{ECP}}(\hat{\mathbf{k}}) = \sum_{j\in\mathcal{S}_n} \sigma_j \int_0^{t_0(E_0)} \mathrm{d}t\, \bar{\lambda}(t) |\Psi_{\hat{\mathbf{k}}}(\mathbf{r}_j; E_0, t)|^2, \quad \text{with}$$

$$\bar{\lambda}(t) \equiv \frac{\lambda(z)}{N t_0(E_0)}. \tag{5}$$

Therefore, the master pattern approach is quite well suited for the ECP case as well. For standard geometry EBSD/TKD patterns and ECPs the master pattern is computed only once for a given crystal structure and microscope voltage, and can be used to compute individual patterns by interpolation.

TKD master pattern simulations proceed along lines similar to the previously published EBSD [1] and ECP [2] modeling approaches. A uniform grid of points is generated on a spherical surface surrounding a hypothetical spherical crystal located at the center; each sampling point represents one outgoing beam direction **k**, and the radius of the sphere is the maximum integration depth $t_0(E)$. The sampling scheme employs the modified Lambert projection introduced in [1,23] in which a uniform grid on a square is mapped onto the sphere by means of an equal-area projection. For each beam direction, and for a given sample thickness, one carries out the integrals of Eq. (2), using the Monte Carlo $\lambda(E, t)$ weighting function determined for that sample thickness. In the following section, we show example TKD master patterns and compare them to similar patterns for the EBSD and ECP modalities.

3. Results

3.1. Comparison between EBSD, ECP, and TKD master patterns

The master pattern expression in Eq. (2) reveals that EBSD, ECP, and TKD master patterns have a lot in common; in particular, the dynamical scattering process that underlies the generation of Kikuchi bands is identical for the three diffraction modalities. The only differences occur in the directional, depth, and energy distributions of the B/FSEs that contribute to the patterns. To illustrate the similarity of the master patterns, Fig. 5 shows a portion of the upper right quadrant (centered on the [111] pole) of the energy-weighted silicon master patterns for (a) ECP, (b) and (c) TKD for two different foil thicknesses (50 and 250 nm) and (d) EBSD. The microscope voltage is 20 kV for all patterns, with a specimen tilt angle of 70° for EBSD, 0° for ECP, and −20° for TKD. The patterns are very similar but differ in small details. The TKD master patterns are plotted with added colour in order to highlight subtle differences. Fig. 5(e) shows line scans through each of the master patterns, slightly vertically offset to make the profiles more clearly visible. The differences in details across the patterns is seen here distinctly. The scan across the ECP pattern in Fig. 5(a) displays significantly better resolved peaks compared to the EBSD one Fig. 5(d), supporting the better resolution observed in the ECP master pattern. Since the main signal in the ECP case consists of BSE1 electrons which have lost only a small amount of energy in the sample before being backscattered, one can consider ECPs to be energy-filtered versions of EBSPs.

The line scans across the TKD patterns for different thickness films are more similar to each other, except for the shift in peaks in the zone axis (highlighted by the grey box). It is rather apparent that both the peak positions and the sharpness of the thin film (50 nm) TKD pattern are more similar to the ECP pattern, while the peaks and blurriness of the thick film TKD pattern are closer to those of the EBSPs. We explain this behaviour by considering the energy loss of electrons contributing to the patterns in each case. The Monte Carlo predicted energy loss spectra for all four cases described above are shown in Fig. 5(f) as fitted Poisson distribution curves. Thin film TKD patterns are produced by electrons with an energy range very close to the ECP case. Similarly, increasing the sample thickness causes the electron exit energy distribution to become wider and shift to lower energies, which corresponds to a broadening and slight blurring of the Kikuchi bands due to the increased Bragg angles; these phenomena are common to EBSPs and thick films TKD patterns.

It becomes apparent that the sample thickness can be seen as an energy filtering mechanism in TKD. In terms of the traditional Hough-based indexing approach, one must thus select a butterfly mask of the appropriate width, depending on the sample thickness and incident electron energy. For the dictionary indexing approach, illustrated in Section 3.3, the pattern dictionary must be computed using the appropriate Monte Carlo and master pattern data, to ensure accurate matches between experimental and simulated patterns.

The EBSD master pattern is an energy-weighted average of individual master patterns and the integration over the electron energy gives rise to a continuous range of Bragg angles and, thus, a general blurring of the master pattern features compared to the ECP case. This will also be the case for individual diffraction patterns that are extracted from the master patterns via bilinear interpolation, as explained in [1].

3.2. Comparison with experimental patterns

Fig. 6 shows two experimental TKD patterns (left column) for a nano-crystalline Aluminum sample, acquired at 30 kV with a sample tilt of −18° in a FEI Teneo field emission scanning electron microscope, using the TSL Hikari EBSD detector system; the sample foil is approximately 150 nm thick. Monte Carlo and master pattern simulations were carried out for these parameters. The detector parameters and grain orientations were obtained through an in-house developed interactive fitting routine, written in the Interactive Data Language [24]; an initial approximate grain orientation is obtained by visually comparing the simulated TKD pattern with the experimental pattern. Once a reasonable orientation is obtained, the detector parameters are refined by using a downhill simplex routine to minimize a cost function, either the normalized dot product between the two patterns or their mutual information. When a reasonable set of parameters is obtained, the grain orientation is refined, and the process is repeated until both detector parameters and grain orientation are satisfactory. This process was applied to the pattern in Fig. 6(a), and the resulting detector and orientation parameters are listed in Table 1.

The same detector parameters were then used to refine the orientation of the pattern in Fig. 6(b). The resulting simulated patterns are shown in the right column of Fig. 6. Note that the only adjustments to the simulated patterns were brightness and contrast changes to maximize the visual agreement between the simulated and experimental patterns. The overall intensity gradient

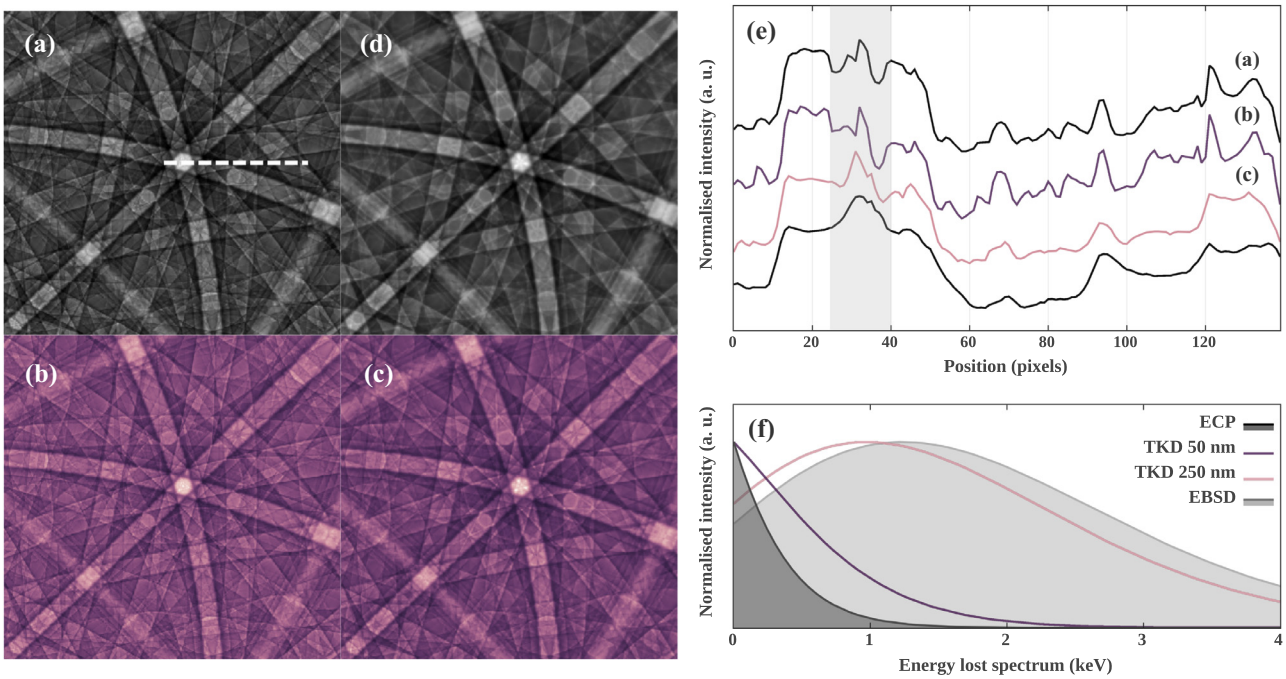

Fig. 5. Portion of the stereographic projection, centered on the [111] pole, of a master pattern for silicon for (a) ECP, (b) and (c) TKD for sample thicknesses of 50 and 250 nm and (d) EBSD. The profiles in (e) represent the intensity along the central line (marked as a dashed line in (a)), for all four cases; the profiles have been offset vertically to make them more visible. The energy loss distribution estimated by the MC model for all four cases is shown in (f) as Poisson distribution fitted curves.

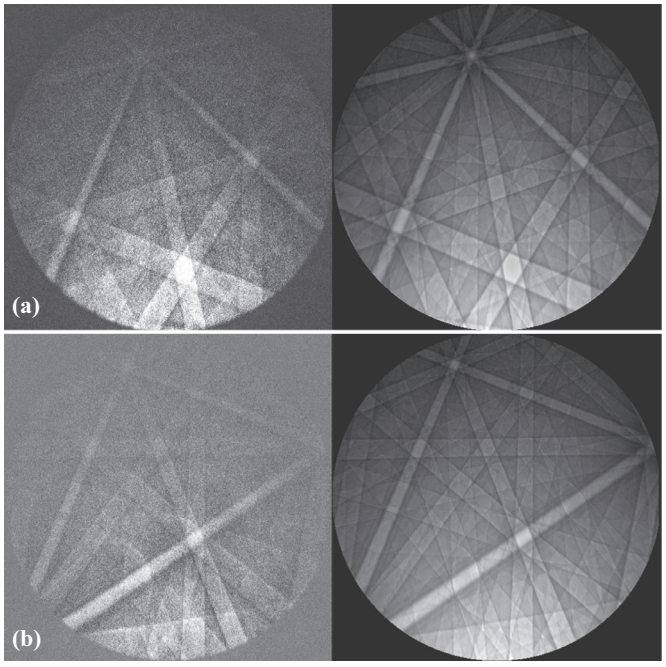

Fig. 6. (left column) Experimental TKD patterns for Aluminum at 30 keV and (right column) corresponding simulated patterns; brightness and contrast of the simulated patterns have been adjusted to better match the experimental patterns. Simulation parameters for both (a) and (b) are stated in the text. The dot product values between normalized patterns are equal to 0.881 for the top pair and 0.834 for the bottom pair, indicating a satisfactory match.

(from bright at the bottom of the pattern to dark at the top) follows directly from the use of the direction-dependent Monte Carlo statistical data, and is in good agreement with the intensity gradients of the experimental patterns. The satisfactory agreement between simulated and experimental patterns indicates that the energy-weighted dynamical scattering model employed in the pattern simulations is sufficient to obtain realistic pattern simulations.

Table 1
Fixed and fitted parameters for the TKD patterns shown in Fig. 6; the detector parameters are listed in the traditional (x^*, y^*, z^*) notation used by commercial EBSD packages (distances in units of the detector width), as well as the units used by the TKD simulations, which express the pattern center location in units of pixels with respect to the center of the detector and the detector-sample distance L in micrometers. The Euler angles (φ_1, Φ, φ_2) use the Bunge zxz convention.

Fixed parameters	
Accelerating voltage [kV]	30.0
Sample tilt [°]	−18.0
Sample thickness [nm]	150.0
Detector pixels size [μm]	70.0
Number of detector pixels	480 × 480
Fitted Parameters	
x^* (x_{pc} [pixels])	0.5134 (6.4406)
y^* (y_{pc} [pixels])	1.0504 (264.1950)
z^* (L [μm])	0.6985 (23, 471.48)
Euler angles (a) [°]	(204.20, 57.54, 209.26)
Euler angles (b) [°]	(119.44, 46.15, 236.72)

3.3. Dictionary indexing of TKD patterns

The recently developed open-source dictionary indexing approach [19], an alternative to the commercially available Hough-based pattern indexing algorithms, is based on the ability to compute a library (dictionary) of diffraction patterns for a uniform sampling of orientation space and a given set of geometrical detector parameters. The technique has been applied successfully to EBSPs [25] and ECPs [2], and in this section we describe the first application of dictionary-based indexing to TKD patterns.

A 30 kV TKD data set was acquired from a nano-crystalline Al sample approximately 150 nm thick. The sample was made by

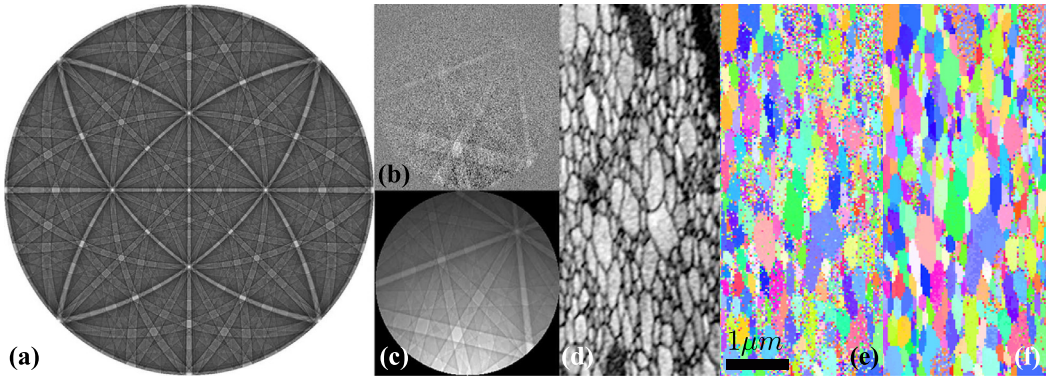

Fig. 7. (a) TKD master pattern for Al at 30 kV for a foil thickness of 100 nm; (b) selected experimental pattern used for the detector parameter determination; (c) simulated pattern corresponding to (b); (d) orientation similarity map (see text for details); (e) [010] inverse pole figure (IPF) obtained with the commercial OIM -8 indexing software; and (f) [010] IPF obtained using the dictionary indexing approach.

DC magnetron sputtering Al on a Ag seed layer deposited on a (111) Si substrate; for details see [26,27]. Foils for performing TKD were shaped using e-beam lithography, then released by etching the substrate with XeF_2. Final removal was done using standard FIB liftout techniques on an FEI Helios dual beam FIB-SEM. The sample was mounted on a 38° pre-tilted holder and the microscope stage was tilted 20° so that the sample was tilted at 18° toward the EBSD detector, which was tilted at 8° from the vertical orientation. TKD was performed on an FEI Teneo SEM FEG-SEM, equipped with an EDAX/TSL Hikari EBSD camera with 480×480 pixels of size of 70 µm. The small data set consists of 86×196 sampling points with a 30 nm step size, resulting in a field of view of 2.58×5.88 µm^2, and each TKD pattern was binned by a factor of $2\times$ to a size of 240×240 pixels. The patterns were first indexed in real-time using the EDX OIM-8 indexing software [28], resulting in an indexing success rate of 95.6%.

A TKD master pattern, shown in Fig. 7(a), was computed using the approach described in Section 2, and orientation space was uniformly sampled using the cubochoric sampling approach described in [13,29], to obtain an orientation set consisting of 333,227 unique orientations inside the cubic Rodrigues fundamental zone; this corresponds to a sampling of orientation space with an average angular step size of 1.4°. The pattern shown in Fig. 7(b) was used to refine the detector parameters using the approach described in Section 3.2 and used along with the TKD master pattern to index the experimental patterns; the corresponding simulated pattern is shown in Fig. 7(c). The experimental and simulated TKD patterns were pre-processed (high-pass filter, followed by adaptive histogram equalization [30]) before computation of the dot products; pre-processing, computation of the 333,227 simulated patterns, and indexing of the 16,856 experimental patterns took a total of 35 min on 24 Intel Xeon E5-2670 2.30 GHz CPU threads (for the pattern simulation) and an NVidia GeForce GTX 1080 GPU (for the dot product calculation). The resulting orientations and related information were exported to both a binary HDF5 file and a CTF file for further processing. The bulk of the computation time is spent on the simulated patterns; pre-computing those patterns and storing them in a file would significantly speed up the indexing process.

Fig. 7(d) shows an orientation similarity map. The dictionary indexing approach produces a list of the top N best matches (dictionary patterns with the N highest dot products, where N is typically set to 30). For each sampling point, the orientation similarity is computed by determining the average number of top matches that this sampling point has in common with its four nearest neighbors; this value is then displayed as a gray scale image, as shown in Fig. 7(d). Since sampling points near grain boundaries will have fewer best matches in common with their neighbors, the orientation similarity map (OSM) provides an easy overview of the microstructure in which grain interiors have a uniform intensity level and all grain boundaries have lower intensity.

The [010] inverse pole figures in Fig. 7(e) and (f) were obtained by the standard commercial OIM-8 indexing package (e) and the dictionary indexing approach (f). The dark regions near the top of the field of view in Fig. 7(d) correspond to surface contamination from the XeF_2 etching step and result in clusters of incorrectly indexed or unindexable points in both indexing approaches; patterns were deemed to be unindexable when either the Image Quality was low (according to the commercial software analysis package) or the Pattern Sharpness parameter, as defined in [31], was low. Overall, the dictionary indexing approach has fewer incorrectly indexed points, in particular near grain boundaries.

4. Discussion and conclusions

Inelastic scattering, a phenomenon usually discarded in diffraction simulations, has direct influence on the energy distribution of diffracting electrons and, consequently, on the imaged Kikuchi patterns. The broader the energy distribution of diffracting electrons, the more diffuse the Kikuchi band edges. Using a Monte Carlo model we can observe that the length of electron trajectories before diffraction is a determining factor in the broadening of the energy distribution. This factor, in turn, can be controlled in the Transmission Kikuchi Diffraction modality through the thickness of the sample, acting effectively as an energy-filtering mechanism. Another determining factor for the energy distribution is the sample-detector geometry which influences both TKD and EBSD modalities.

We should note that the Monte Carlo model used in this work explicitly describes the lower escape distance values for the signal carrying electrons. A subset of electrons reaching the detector will, nevertheless, carry a probability of channeling over longer trajectories. Depending on their travel direction inside the crystal, these electrons are expected to give rise to contrast inversion of one or more Kikuchi bands (observed as dark instead of bright lines). This will occur when the distance traveled is of the order of, or larger than, the extinction distance for a particular plane. Contrast inversions are thus expected to occur for both EBSD and TKD modalities when the sample is tilted such that long electron trajectories are possible; in addition, the sample should have a crystal structure that gives rise to short extinction distances. For the ECP modality, contrast inversions are not expected to occur unless very large sample tilt angles are used, which is not practical due to the possibility of the sample hitting the back-scatter detector. Similarly,

when the TKD detector if mounted horizontally, below the sample, the electron trajectories inside the sample will have a narrow range of escape distances, so that contrast inversions are also not expected to occur. A statistical model more sensitive to the outlier cases of long distance channeling electrons is therefore necessary if we are to correctly predict band contrast inversion.

The energy-weighted scattering model is shown to correctly predict Kikuchi bands sharpness (defined as signal to noise intensity) for the different SEM modalities. When used for the dictionary indexing approach it was shown to produce indexed TKD patterns with fewer incorrectly indexed points compared to commercial Hoigh transform based indexing software.

Acknowledgements

The authors would like to thank Professor Xinghang Zhang for providing the nano-crystalline Al and D.S. Gianola and E. Yao for helpful discussions. EP would like to acknowledge SUPA for travel support and EPSRC and NPL for funding; SS and MDG acknowledge a Vannevar Bush Fellowship, ONR # N00014-16-1-2821, for financial support; PC acknowledges ONR N00014-16-1-2982 for financial support. The authors would also like to acknowledge the instrumentation and computational facilities of the Materials Characterization Facility at Carnegie Mellon University under grant # MCF-677785.

Supplementary material

Supplementary material associated with this article can be found, in the online version, at 10.1016/j.ultramic.2018.01.003.

References

[1] P. Callahan, M. De Graef, Dynamical EBSD patterns part I: pattern simulations, Microsc. Microanal. 19 (2013) 1255–1265.
[2] S. Singh, M. De Graef, Dictionary indexing of electron channeling patterns, Microscosc. MicroAnal. 23 (2017) 1–12.
[3] A. Schwartz, M. Kumar, B. Adams, D. Field (Eds.), Electron Backscatter Diffraction in Materials Science, Springer, 2009.
[4] A. Winkelmann, G. Nolze, S. Vespucci, G. Naresh-Kumar, C. Trager-Cowan, A. Vilalta-Clemente, A. Wilkinson, M. Vos, Diffraction effects and inelastic electron transport in angle-resolved microscopic imaging applications, J. Microsc. 267 (2017) 330–346.
[5] R. Keller, R. Geiss, Transmission EBSD from 10 nm domains in a scanning electron microscope, J. Microsc. 245 (2011) 245–251.
[6] P.W. Trimby, Orientation mapping of nanostructured materials using transmission Kikuchi diffraction in the scanning electron microscope, Ultramicroscopy 120 (2012) 16–24.
[7] D. Joy, Channeling in and channeling out: the origins of electron backscattering and electron channeling contrast, in: Proceedings of the annual meeting-Electrons Microscopy Society of America, San Francisco Press, 1994, pp. 592–593.
[8] D. Coates, Kikuchi-like reflection patterns obtained with scanning electron microscope, Philos. Mag. 16 (144) (1967) 1179–1185.
[9] D. Joy, D. Newbury, D. Davidson, Electron channeling patterns in the scanning electron microscope, J. Appl. Phys. 53 (1982).
[10] L. Reimer, Scanning Electron Microscopy – Physics of Image Formation and Microanalysis, Springer, Berlin, 1998.
[11] A. Winkelmann, C. Trager-Cowan, F. Sweeney, A. Day, P. Parbrook, Many-beam dynamical simulation of electron backscatter diffraction patterns, Ultramicroscopy 107 (2007) 414–421.
[12] Y. Picard, M. Liu, J. Lammatao, R. Kamaladasa, M. De Graef, Theory of dynamical electron channeling contrast images of near-surface crystal defects, Ultramicroscopy 146 (2014) 71–78.
[13] S. Singh, M. De Graef, Orientation sampling for dictionary-based diffraction pattern indexing methods, Modell. Simul. Mater. Sci. Eng. 24 (2016).
[14] A. Howie, Inelastic scattering of electrons by crystals I. The theory of small-angle inelastic scattering, Proc. R. Soc. Lond. A 271 (1963) 267–287.
[15] A. Winkelmann, G. Nolze, M. Vos, F. Salvat-Pujol, W. Werner, Physics-based simulation models for EBSD: advances and challenges, IOP Conf. Ser. 109 (1) (2016) 012018.
[16] H. Yoshioka, Effect of inelastic waves on electron diffraction, J. Phys. Soc. Japan 12 (1957) 618–628.
[17] B.D. Forbes, Thermal diffuse scattering in transmission electron microscopy, Ultramicroscopy 111 (2011) 1670–1680.
[18] D. Joy, Monte Carlo Modeling for Electron Microscopy and Microanalysis, Oxford University Press, USA, 1995.
[19] Y. Chen, P. S.U., D. Wei, G. Newstadt, M. Jackson, J. Simmons, M. De Graef, A. Hero, A dictionary approach to EBSD indexing, Microsc. Microanal. 21 (2015) 739–752.
[20] D.C. Joy, S. Luo, An empirical stopping power relationship for low-energy electrons, Scanning 11 (1989) 176–180.
[21] D. Scott, Multivariate Density Estimation: Theory, Practice, and Visualization, John Wiley & Sons, New York, Chicester, 1992.
[22] K.P. Rice, R.R. Keller, M.P. Stokyovich, Specimen thickness effects on transmission Kikuchi patterns in the scanning electron microscope, J. Microsc. 254 (2014) 129–131.
[23] D. Roşca, New uniform grids on the sphere, Astron. Astrophys. 520 (2010) A63.
[24] E.V.I. Solutions, Interactive data language (version 8.6), 2016. URLhttps://search.library.wisc.edu/catalog/9910207172502121.
[25] K. Marquardt, M. De Graef, S. Singh, H. Marquardt, A. Rosenthal, T. Hiraga, Quantitative electron backscatter diffraction (EBSD) data analyses using the dictionary indexing (DI) approach: overcoming indexing difficulties in geological materials, Am. Mineral. (2017). (in press)
[26] D. Bufford, H. Wang, X. Zhang, High strength, epitaxial nanotwinned Ag films, Acta Mater 59 (1) (2011) 93–101.
[27] D. Bufford, Y. Liu, Y. Zhu, Z. Bi, Q. Jia, H. Wang, X. Zhang, Formation mechanisms of high-density growth twins in aluminum with high stacking-fault energy, Mater. Res. Lett. 1 (1) (2013) 51–60, doi:10.1080/21663831.2012.761654.
[28] S. Wright, M.M. Nowell, S.P. Lindeman, P.P. Camus, M. De Graef, M.A. Jackson, Introduction and comparison of new EBSD post-processing methodologies, Ultramicroscopy 159 (2015) 81–94.
[29] D. Roşca, A. Morawiec, M. De Graef, A new method of constructing a grid in the space of 3D rotations and its applications to texture analysis, Model. Simul. Mater. Sci. Eng. 22 (2014) 075013.
[30] S. Pizer, E. Amburn, J. Austin, R. Cromartie, A. Geselowitz, T. Greer, B. Romney, J. Zimmerman, K. Zuiderveld, Adaptive histogram equalization and its variation, Comput. Vision, Graph. Image Process. 39 (1987) 355–368.
[31] N. Krieger Lassen, D. Juul Jensen, K. Conradsen, On the statistical analysis of orientation data, Acta Crystallograph. A 50 (1994) 741–748.